Chemical Engineering Journal 520 (2025) 165913

Contents lists available at ScienceDirect

Chemical Engineering Journal

journal homepage: www.elsevier.com/locate/cej

Three-dimensional computational fluid-dynamic simulation of sorption enhanced gasification☆

Alessandro Antonio Papa [a], Armando Vitale [a,*], Umberto Pasqual Laverdura [b], Antonio Di Nardo [b], Giorgio Calchetti [b], Andrea Di Carlo [a], Sergio Rapagnà [c]

[a] Industrial Engineering Department, University of L'Aquila, Piazzale E. Pontieri 1, Monteluco di Roio, 67100 L'Aquila, Italy
[b] Dipartimento di Tecnologie Energetiche e Fonti Rinnovabili, ENEA Centro di ricerche Casaccia, Via Anguillarese, 391, Santa Maria di Galeria, 00123 Roma, Italy
[c] University of Teramo, via R. Balzarini 1, 64100 Teramo, Italy

ARTICLE INFO

Keywords:
Sorption enhanced gasification
Devolatilization
Computational particle fluid dynamic simulation
Hydrogen

ABSTRACT

This study presents a three-dimensional computational particle fluid dynamic (CPFD) simulation of sorption-enhanced gasification (SEG) using almond shells as feedstock. A detailed biomass characterization, including devolatilization behavior and gasification at two different steam-to-biomass ratios, was conducted. The devolatilization tests were performed at a temperature between 600 and 850 °C to derive the kinetic of this fundamental step. Then gasification tests were performed using a lab-scale fluidized bed reactor. A mixture of olivine and dolomite served as the bed material. Experimental data, including gas yield, tar formation, and hydrogen production, were used to tune and validate the CPFD model. Results showed that increasing the steam-to-biomass ratio from 0.5 to 1.0 increased hydrogen yield from 70.2 % to 78.8 %. In contrast, gas yield increased from 0.76 to 0.80 Nm^3/kg confirming the positive impact of the in-situ CO_2 capture on syngas quality with tar content ranging from 9.5 to 11.6 g/Nm^3. Char yield decreased from 39.6 % to 36.0 %. The model closely predicted gasification behavior, though some discrepancies in tar formation were observed.

1. Introduction

The global transition towards cleaner and renewable energy sources has intensified interest in biomass and waste materials as carbon-neutral alternatives in the fossil-based energy infrastructure and a sustainable option for producing bio-based materials [1,2]. According to the International Energy Agency, achieving net-zero emissions by 2050 will require bioenergy to account for up to 20 % of the global energy supply [3].

Gasification represents a promising technology for converting organic material into syngas, a valuable fuel mixture primarily composed of H_2, CO, CO_2, and CH_4 [4]. Among gasification processes, steam gasification is particularly notable for its ability to produce hydrogen-rich syngas [5]. Utilization of the product gas for heat and power production is already supported by various renewable energy schemes [6]. Furthermore, syngas can be used to synthesize products such as synthetic natural gas (SNG), Fischer-Tropsch fuels (e.g., aviation fuels), and chemical building blocks [7,8].

Gasification also holds significant potential for bio-hydrogen production, offering an economically viable pathway [9,10]. However, thermodynamic equilibrium limits conventional biomass gasification, restricting hydrogen yield and leading to diluted hydrogen due to the formation of CO, CO_2, and CH_4 [11].

Sorption Enhanced Gasification (SEG) has been proposed as a promising process that integrates CO_2 capture during gasification, shifting the equilibrium of key reactions, such as the water-gas shift (WGS), towards increased H_2 production [12,13]. This process uses solid sorbents, such as CaO, which undergo cyclic carbonation and calcination to capture and release CO_2 during gasification, allowing the in-situ removal of CO_2, enhancing hydrogen production while also reducing tar formation [12].

A dual-fluidized bed (DFB) gasification system, which couples a carbonator/gasifier and calciner/combustor reactors, enables feedstock conversion at temperatures between 600 and 700 °C, while capturing CO_2 with the CaO sorbent. The sorbent is regenerated in a separate reactor operating at 800–900 °C, where the captured CO_2 is released.

☆ This article is part of a Special issue entitled: ‘ISCRE 28’ published in Chemical Engineering Journal.

* Corresponding author.
E-mail address: armando.vitale@graduate.univaq.it (A. Vitale).

https://doi.org/10.1016/j.cej.2025.165913
Received 19 November 2024; Received in revised form 8 July 2025; Accepted 10 July 2025

SEG offers several advantages over conventional gasification, including higher hydrogen yields and the ability to operate at lower temperatures, thereby reducing energy consumption. Lower operating temperatures in SEG limit the char gasification, resulting in lower gas yields but allowing increased char recirculation to the combustor, reducing the need for auxiliary fuel. Additionally, the H_2-to-CO ratio in the product gas can be controlled by adjusting the process temperature or the bed material circulation rate [14].

However, the cyclic of carbonation and calcination presents challenges such as sorbent deactivation due to sintering and attrition, gradually reducing CO_2 capture efficiency [15]. Recent studies have focused on improving the longevity and reactivity of CaO-based sorbents by introducing dopants or using alternative materials like dolomite [16,17]. Furthermore, the optimizing operational parameters, such as the steam-to-biomass ratio (S/B), gasification temperature, and bed material circulation rates, plays a critical role in maximizing hydrogen yield and minimizing char and tar formation [18].

While experimental research provides valuable insights into the SEG process, capturing the complex multiphase interactions between feedstock particles and devolatilization, fluidized bed material, gaseous species, and CO_2 capture remains challenging. Computational Particles Fluid Dynamics (CPFD) enables the simulation of flow patterns, process kinetics, fluid dynamics, thermodynamics of the process under various conditions, and particle-fluid interactions in ways that are difficult to achieve through experiments alone [19–22]. Accurately modelling these interactions is essential for the designing, optimizing, and scaling-up of fluidized bed reactors [23].

The CPFD method, implemented in Barracuda VR® software, is based on the MP-PIC model and employs a Lagrangian-Eulerian approach. In this framework, the gas phase is treated as a continuous fluid characterized by its own density, temperature, and velocity, while the solid phase is modeled as a discrete Lagrangian entity. The two phases are fully coupled, accounting for interactions such as turbulence, heat, mass, and momentum exchanges between the solid and fluid phases. Particles are categorized by size, species, and other factors, and collisions are modeled as spatial gradients on the Eulerian grid using an isotropic solid stress function, which is then interpolated onto the discrete particles. The stress function is influenced by the solid volume fraction, and accurate interpolation requires that the size of the physical particles be small relative to the Eulerian grid. This method allows the simulation of various fluid-solid flow regimes, ranging from bubbling near the close-packing limit to more dilute conditions. One advantage of this model is that particles move independently, enabling the use of GPU parallel processing. Additionally, the approach supports larger time steps, making long-term simulations more feasible, as the CPFD method can operate on coarse grids without sacrificing accuracy.

Barracuda® is currently used by many research groups to study reactive processes in fluidized beds. These studies show that the software is universally accepted as a tool for investigating such processes, providing results that are consistent with experimental data and offering valuable insights for understanding the various phenomena.

Kraft et al. [19] modeled an 8 MWth steam gasification dual fluidized bed. The model successfully predicted product and flue gas compositions, as well as temperature profiles, with reasonable precision. Zhu et al. [21] successfully numerically investigated biomass gasification with CO_2 in a pilot plant circulating fluidized bed (CFB) gasifier via a reactive multiphase particle-in-cell (MP-PIC) model by means of Barracuda VR®. Kong et al. [24] simulated biomass gasification in a three-dimensional pilot-scale dual fluidized bed (DFB) with complex geometric structure by means of Barracuda VR®. The thermochemical behaviors of bed materials and biomass particles were investigated, and the impacts of several key operational parameters (such as temperature, steam-to-biomass ratio, and equivalence ratio) on gasification performance were revealed. Guo et al. [25] simulated a dual fluidized bed, that combines biomass gasification and CO_2 capture, with adsorbent regeneration, by means of Barracuda VR®. They analyzed the influence of several key operating parameters on gasification performance and the adsorbent content. The mole fraction of H_2 increased by 54.6 % compared to the process without capture. Liu et al. [26] evaluated the influence of the particle size distribution and the drag model, in a three-dimensional dual fluidized-bed biomass gasifier, using Barracuda VR®. The model predicted the gas composition and the reactor temperature distribution in comparison to experimental data.

CPFD simulations results particularly valuable for studying sorption-enhanced processes because it allows to consider the CO_2 continuously removed from the gas phase and the contemporary formation of $CaCO_3$ within the bed, which is essential to evaluate the performance of the process and for understanding the sorbent circulation rate and regeneration needs. Furthermore, the effect of S/B on the extent of the reaction, the efficiency of CO_2 capture, and the composition of syngas can be evaluated [25].

Accurately modelling reaction kinetics, including devolatilization, primary gasification reactions, and secondary CO_2 sorption reactions, is critical to predicting SEG system performance under different conditions. A major advantage of CPFD is its ability to integrate experimental data into predictive models. For example, experimental results on devolatilization and syngas composition can be used to validate CPFD models, ensuring they reflect real-world behavior [22].

By integrating experimental data with CPFD simulations, this study aims to deepen understanding of the SEG process, identify optimal operating conditions, and provide guidance for the scale-up and implementation of gasifier reactors with calciners. The experimental tests focus firstly on biomass devolatilization, emphasizing the kinetic, distribution and composition of gas, char, and tar produced. Gasification tests were conducted in a laboratory-scale reactor. These experiments provide detailed input data for the CPFD model, developed using Barracuda software.

The CPFD model is tuned and validated using experimental data. This approach ensures that the model accurately predicts the SEG process behavior and can be used to explore a wide range of operating conditions, allowing for optimization without the need for costly and time-consuming experiments.

2. Material and methods

2.1. Material

Almond shells with an average particle size of approximately 1.5 mm were used for the tests. The characterization of the material is reported in Table 1.

Thermogravimetric analysis (TGA) was performed to determine moisture, volatile matter and ash content using a Linseis STA 1000, following the ASTM D7582 standard. A PerkinElmer 2400 Series II elemental analyser was used to determine the C, H, N, S contents in accordance with the ASTM D3178 standard. The oxygen content was estimated by difference.

Table 1
Characterization of almond shells.

Particle density	613.5	kg/m^3
Proximate analysis		
Moisture	7.69	$wt\%_{dry}$
Volatile matter	70.62	$wt\%_{dry}$
Fixed carbon	20.21	$wt\%_{dry}$
Ash	1.48	$wt\%_{dry}$
Ultimate analysis		
C	49.90	$wt\%_{dry\_ashfree}$
H	6.30	$wt\%_{dry\_ashfree}$
N	0.51	$wt\%_{dry\_ashfree}$
S	0.02	$wt\%_{dry\_ashfree}$
O	43.27	$wt\%_{dry\_ashfree}$

2.2. Devolatilization setup and tests procedure

The devolatilization behavior of the material was studied by using the test rig represented in Fig. 1. The complete description of the system is reported in a previous work [27].

The system consists of a fluidized bed reactor with inert quartz sand (Sauter Diameter, $d_{3,2} = 250$ μm) that works at the same fluidization velocity of the gasifier (twice the minimum fluidization velocity, u_{mf} (m/s)) to reproduce similar conditions in terms of heat and mass transfer.

Two K-type thermocouples were used to monitor the bed temperature (T1) and outlet gas temperature (T2). T1 is used to properly program the electric oven to maintain the bed at the process temperature, while T2 is used to set a heating tape in order to maintain the outlet tube at temperature as high as to avoid the condensation of heavy compounds.

Nitrogen or air is used as fluidization agents during the devolatilization and combustion phases, respectively. The flow rates were regulated by Mass flow controller (MFC—Bronkhorst El Flow Select).

The devolatilization tests were conducted by feeding the material directly into the fluidized bed from above according to the following two procedures:

- Batch tests at 600, 725, and 850 °C determining the devolatilization times versus temperature.
- Semi-continuous feed tests at 670 °C to derive the product composition in terms of syngas volume fractions, tar and char.

To derive the devolatilization time, several batches are injected into the reactor. Between one injection and the next, the output gas flow rate stabilizes to the initial nitrogen flow rate. The outlet flow rate and pressure trends are measured and analyzed.

By performing the same procedure for each temperature, the decomposition times trend is obtained. The data are then used to derive the kinetic expression according to the procedure already developed in a previous work [28].

The complete analysis of the product released during the devolatilization phase for almond shells is obtained with semi-continuous tests on the devolatilization test rig that consists of the injection of batches of material every 30 s for 25 min; then the fluidization agent switched from nitrogen to air for the combustion phase to burn and quantify all the residual char. The produced gas flow rate was measured during both phases of the test using a mass flow meter (MFM – Bronkhorst®) while the composition was analyzed using ABB online analyzers (Caldos and Uras). In particular, H_2, CO, CO_2 and CH_4 were detected during the devolatilization phase, while CO and CO_2 during the combustion phase.

Downstream the reactor, the gas flows through a series of impinger bottles filled with organic solvent (isopropanol) maintained at −10 °C to solubilize the aromatic hydrocarbons. After the test, a sample of the solution was collected for offline analysis with GC–MS (Agilent 7890) to identify and quantify the aromatic compounds produced.

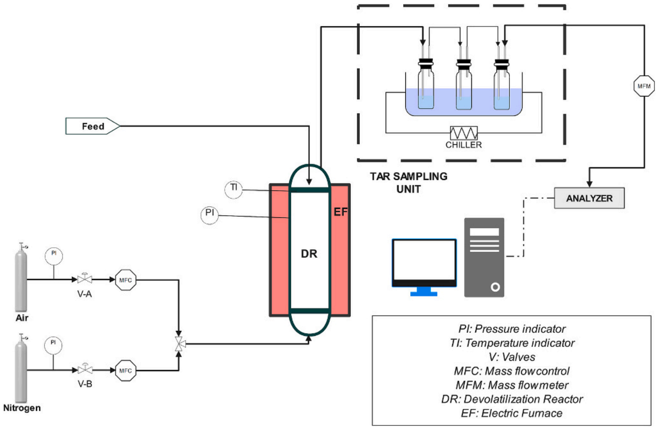

Fig. 1. Devolatilization bench scale rig [27].

A slipstream of the produced gas was collected during the devolatilization step to perform offline analysis for the detection of C2-C4 compounds by using a Micro-GC (Agilent 990).

2.3. Gasification setup and tests procedure

Fig. 2 shows a schematic representation of the lab-scale gasification test rig used for the tests. A complete description of the system is reported in [22].

The system includes a fluidized bed reactor (ID = 10 cm and h = 85 cm) with a mixture of olivine and calcined dolomite as bed material (50 wt%). Table 2 reports the main characteristics of the bed materials and the relative minimum fluidization rate and fluidizing agent flow rate used for the test.

Three K-type thermocouples are inserted in the bed, freeboard and outlet gas to monitor the system temperature during the test. Moreover, the bed temperature is used to set the electric oven for heating up the reactor.

A mixture of nitrogen and steam was used as gasifying agent with the flow rates regulated by a mass flow controller (MFC - Bronkhorst El Flow Select) and a peristaltic pump, respectively.

The biomass was fed to the reactor from the upper part by means of a screw conveyor.

Table 3 reports the operating conditions used for the test.

The produced gas was cooled, and the residual steam condensed downstream of the reactor by a series of condensers maintained at 274 K. A vacuum pump enabled gas circulation in the plant (VP1).

The dried syngas was continuously analyzed by online ABB analyzers for the detection of H_2, CO, CO_2, CH_4, while the flow rate was measured by mass flow meter (MFM – Bronkhorst®).

Once the system reached steady state, the vacuum pump (VP2) was used to spill 1 Nl/min of syngas through the tar sampling unit. This unit consists of a series of impinger bottles with isopropanol, maintained at 40 °C and −10 °C (in accordance with CEN/TS 15439 standard), to solubilize the aromatic compounds produced. As in the devolatilization tests, a solution sample was collected for offline analysis using GC–MS (Agilent 7890).

Moreover, during steady-state operation, a gas sample was collected for offline analysis with an Agilent 990 Micro-GC to evaluate light hydrocarbons.

Before each test, the reactor was initially fed with air during the heating phase until the operating temperature was reached. Subsequently, the air was replaced with a steam-nitrogen mixture. The test began after detecting the water drop from the first condenser, and it can be subdivided into three phases:

- Sorption-enhanced gasification
- Calcination of the bed material at 900 °C
- Combustion of the remaining char

At the end of the gasification phase, condensed water was recovered and measured to evaluate the average water content in the syngas. Next, calcination of dolomite was performed by heating the reactor to 900 °C with nitrogen as fluidizing agent, and the amount of captured CO_2 was determined.

After the calcination phase, unreacted char was quantified by feeding air to the reactor and analyzing the produced gas in terms of flow rate and composition.

To evaluate gasification performance, water conversion, char and gas yield were calculated according to the following equations (Eqs. (1), (2) and (3)).

Water conversion (H_2O_{conv}) was calculated by:

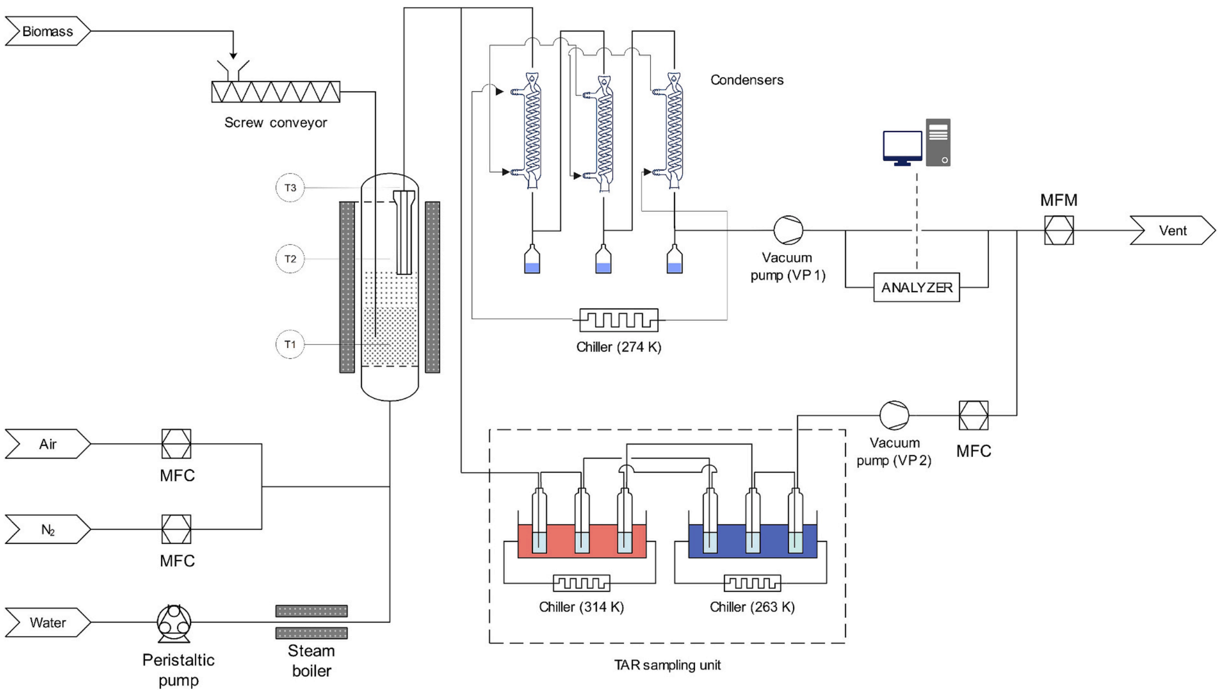

Fig. 2. Gasification bench scale rig [29].

Table 2
Main properties of calcined dolomite and olivine used as bed material.

Material	Calcined dolomite	Olivine
Density (kg/m^3)	1650	3300
Sauter mean diameter (mm)	330	255
Minimum fluidization velocity at 670 °C (m/s)	0.043	0.044
Fluidizing agent flow rate (m^3/s)	8.6 E-4	8.4 E-4

Table 3
Summary of the main gasification test operating condition.

Biomass feed rate	10.6	g/min
Bed temperature	670	°C
Steam to biomass	0.5–1	$kg_{Steam}/kg_{C\_Biomass}$
Water feed	5.4	g/min
Tar sampling duration	30	min

$$H_2O_{conv}(\%) = \frac{m_{H_2O,IN} - m_{H_2O,OUT}}{m_{H_2O,IN}} \tag{1}$$

where $m_{H_2O,IN}$ (kg) is the sum of the steam fed into the reactor and the moisture of the biomass, while $m_{H_2O,OUT}$ (kg) is the water recovered from the condenser.

Gas yield (Y_G) was calculated as:

$$Y_G\left(Nm^3 \Big/ kg_{Biom,dry}\right) = \frac{\dot{Q}_{gass}}{\dot{m}_{Biom,dry}} \tag{2}$$

where $\dot{Q}_{gass}$ is the volumetric flow rate (Nm^3/h) of gas during gasification phase, determined by the total gas flow rate, measured by the mass flow meter, multiplied by the volume fraction of each species as measured by the ABB analyzers, and $\dot{m}_{Biom,dry}$ is the mass flow rate of dry biomass fed to the reactor (kg/h).

The char yield (Y_C) was calculated as:

$$Y_C\left(g_{char} \Big/ kg_{C,Biom}\right) = \frac{\sum_{i=CO,CO_2} n_{i,comb} MW_C}{m_{C,Biom}} \tag{3}$$

where $n_{i,comb}$ is the mole of CO, CO_2 in the outlet gas during the combustion phase, PM_C is the molecular weight of carbon, and $m_{C,Biom}(kg)$ refers to the amount of carbon fed into the reactor (calculated as the biomass feeding rate multiplied by the carbon content of the biomass).

2.4. Computational model

2.4.1. Governing equations

The CPFD method, implemented in Barracuda VR® software, is based on the MP-PIC model and employs a Lagrangian-Eulerian approach [30,31]. In this framework, the gas phase is treated as a continuous fluid characterized by its own density, temperature, and velocity, while the solid phase is modeled as a discrete Lagrangian entity. The two phases are fully coupled, accounting for interactions such as turbulence, heat, mass, and momentum exchanges between the solid and fluid phases. Particles are categorized by size, species, and other factors, and collisions are modeled as spatial gradients on the Eulerian grid using an isotropic solid stress function, which is then interpolated onto the discrete particles. The stress function is influenced by the solid volume fraction, and accurate interpolation requires that the size of the physical particles be small relative to the Eulerian grid. This method allows the simulation of various fluid-solid flow regimes, ranging from bubbling near the close-packing limit to more dilute conditions. One advantage of this model is that particles move independently, enabling the use of GPU parallel processing. Additionally, the approach supports larger time steps, making long-term simulations more feasible, as the CPFD method can operate on coarse grids without sacrificing accuracy.

The CPFD method utilizes the finite volume approach for solving the governing equations. The scalar and momentum equations are discretized on a staggered grid and the time derivative is approximated by a backward difference [31].

Pressure, velocity, and density are interconnected via a pressure equation, which is derived from mass conservation principles, while the ideal gas law is used to relate pressure and density. The default advection scheme in Barracuda® is the second order Partial Donor Cell method [32]. The Partial Donor Cell scheme is a weighted average of central difference and upwind convection. A limiter is applied to automatically weigh the central difference and upwind quantities. The specified time step is effectively a maximum time step since the actual time step may be limited by the CFL number or temperature changes. The defaults for CFL are: values of 0.8 for the min and 1.5 for the max. During each time step, Barracuda VR® uses an iterative solution method to calculate fluid and solid states (pressure, temperature, velocities, etc.) that satisfy the underlying differential equations for mass, momentum, and energy transport. Each iteration that the solver runs will progressively increase the degree to which the differential equations are satisfied, thereby decreasing the error at each point. The summation of errors existing within the solution forms the residual which can be used to determine whether the solution has converged to an acceptable level. The default residuals are: 1e-07 for Volume, 1e-06 for Pressure, 1e-07 for Velocity, 1e-06 for Energy.

To model turbulence, the Large Eddy Simulation (LES) technique is applied [33], with the sub-grid viscosity calculated using the Smagorinsky model [34]. Particle to wall interaction is accounted by momentum normal and tangential retention coefficients, while particle-to-particle interaction is accounted by the Maximum momentum redirection from collision (default 40 %) [34,35]. The software implements a blended drag model defined as Wen and Yu [35] (D_{WY}) and Ergun [36] (D_{Ergun}), and the particle stress model of Harris and Crighton [37] to simulate particle-particle collisions. A blended acceleration model was used to consider the inhibition of relative motion between particles of different sizes or densities [38].

A summary of the equations applied for the MP-PIC method utilized by BARRACUDA VR ® is reported in Table 4.

During the simulation, the variables of interest (outlet gas composition) were monitored. It was seen that after 30 s these quantities reach a constant value over time. Simulations were conducted by means of Barracuda VR® CPFD software, version 20.1.0 (2020), on an ENEA CRESCO® machine with a quad-core Intel® Xeon® E5620 CPU and a NVIDIA TESLA V100-PCIE GPU, utilizing 15,360 CUDA cores and achieving up to 1.43 Teraflops of double-precision and 4.29 Teraflops of single-precision peak performance.

2.4.2. Reaction kinetics

After the introduction of wet biomass into the reactor, the temperature increase leads first to the release of the feedstock moisture. Then, during the devolatilization phase, the thermal decomposition of the main biomass constituents, primarily cellulose, hemicellulose and lignin, progressively produces volatiles. This process involves complex chemical reactions, including the breaking of chemical bonds within the biomass structure, leading to the formation of various gases and solid residues.

It results in the formation of permanent gas species (CO, CO_2, CH_4, H_2), light (non-condensable) hydrocarbons (C_nH_m), condensable species, which include aromatic compounds and water, and carbon-rich solid material (char).

In this study, the drying and devolatilization phases were assumed to occur simultaneously, in a single step, due to the rapid heating rates and the relatively small size of the biomass particles. Although the thermal decomposition of solids is a complex phenomenon that involves highly intricate kinetics, it can be effectively approximated using a first-order kinetic model with apparent parameters that adequately represent the process [39,40].

This approach has been widely applied in the literature and was also employed in a previous study by the authors [28], where a first-order kinetic model was developed to effectively integrating the complex heat transfer phenomena occurring within the particle and between the particle and the fluidized bed.

The use of this simplified kinetic model allows for an accurate fitting of experimental devolatilization times and while ensuring compatibility with simulation software, where first-order kinetics are commonly included as system input parameters.

The kinetic expression for the particle decomposition is provided in Eq. (4):

$$\frac{dm_i}{dt} = -A_i \exp\left(-\frac{E_i}{RT}\right) \cdot m_i A_i = B_i T^{C_i} \tag{4}$$

where T is the temperature (K), m_i is the particle mass (kg), A_i is the pre-exponential factor, and E_i is the activation energy (J/mol). The term C_i accounts for the effect of temperature on the pre-exponential factor.

The product distribution and volatiles composition were derived from experimental tests designed to simulate experimental operating conditions as described above in the previous section. According to the work of [41], the produced water is considered the sum of moisture initially present in the biomass and the pyrolytic water generated during the decomposition of organic compounds.

The mass balance of the devolatilization phase can be represented by the following equations:

$$Biomass \rightarrow \alpha_1 Volatiles + \alpha_2 Char + \alpha_3 Ash \sum \alpha_i = 1 \tag{5}$$

Table 4
Summary of the governing equations for gas and particle phases implemented in BARRACUDA VR ®.

$\frac{\partial(\varepsilon_g \rho_g)}{\partial t} + \nabla\cdot(\varepsilon_g \rho_g \boldsymbol{u}_g) = \delta \dot{m}_p$	Continuity equation gas phase
$\frac{\partial(\varepsilon_g \rho_g \boldsymbol{u}_g)}{\partial t} + \nabla\cdot(\varepsilon_g \rho_g \boldsymbol{u}_g \boldsymbol{u}_g) = -\nabla p - \boldsymbol{F} + \varepsilon_g \rho_g g + \nabla\cdot(\varepsilon_g \tau_g)$	Momentum transfer equation gas phase
$\frac{\partial f_d}{\partial t} + \nabla\cdot(f_d \boldsymbol{u}_p) + \nabla_{u_p}\cdot(f_d \boldsymbol{a}_p) = 0$	Equation for solid phase description
$f_d = (x, u_p, \rho_p, V_p, t)$	Liouville probability distribution function
$\delta \dot{m}_p = -\iiint f_d \frac{dm_p}{dt} dm_p d\boldsymbol{u}_p dT_p$	Equation for source term of continuity equation
$\boldsymbol{F} = \iiint f_d \left(m_p \left[D_p (\boldsymbol{u}_g - \boldsymbol{u}_p) - \frac{1}{\rho_p} \nabla p \right] + \boldsymbol{u}_p \frac{dm_p}{dx} \right) dm_p d\boldsymbol{u}_p dT_p$	Interphase momentum exchange equation
$\varepsilon_p = \iiint f_d \frac{m_p}{\rho_p} dm_p d\boldsymbol{u}_p dT_p$	Particle volume fraction
$\tau = \frac{10 \cdot P_s \cdot \varepsilon_p^{\beta}}{max[(\varepsilon_{cp} - \varepsilon_p), \alpha(1 - \varepsilon_p)]}'$	Solid stress model equation
$D_p = C_D \cdot \frac{3}{8} \cdot \frac{\rho_g}{\rho_p} \cdot \frac{\lvert \boldsymbol{u}_g - \boldsymbol{u}_p \rvert}{r_p}$	Inter-phase drag function
$D_{WYE} = \begin{cases} D_{WY} \\ (D_{Ergun} - D_{WY}) \left(\frac{\varepsilon_p - 0.75\varepsilon_{cp}}{0.85\varepsilon_{cp} - 0.75\varepsilon_{cp}} \right) + D_{WY} \\ D_{Ergun} \end{cases}$ $\varepsilon_p < 0.75\varepsilon_{cp}$ $0.75\varepsilon_{cp} < \varepsilon_p < 0.85\varepsilon_{cp}$ $\varepsilon_p > 0.85\varepsilon_{cp}$	Drag model equation

$$Volatiles \rightarrow Permanent\ gas + Light\ hydrocarbon + Tar + Moisture + Pyrolytic\ water \tag{6}$$

These equations represent the conservation of mass during thermal decomposition. The coefficients $\alpha_1; \alpha_2; \alpha_3$ are the fractions of biomass converted into volatiles, char, and ash respectively. The sum of these coefficients equals one, ensuring that all mass is accounted for.

The devolatilization products undergo several serial and parallel reactions, both among themselves and with the surrounding gases. These secondary reactions can lead to the formation of additional products or the alteration of existing ones. For instance, tar compounds might crack into lighter gases or recombine into more complex structures, depending on the reaction environment [41].

For the gasification phase, both homogeneous gas phase reactions, and heterogeneous reactions, which involve solid materials like dolomite and char, are considered. The reactions and their corresponding kinetics, as taken from the literature, are summarized in Table 5.

In particular, the rate expression for the CO_2 sorption reaction is based on the model developed by Stendardo and Foscolo [49], which used a particle grain model approach to describe the carbonation process. This model is characterized by an exponentially decreasing diffusion coefficient as a function of CaO conversion through the $CaCO_3$ layer produced on the CaO grain and a first-order surface reaction. As carbonation proceeds, the formation of the $CaCO_3$ layer leads to a volumetric expansion of the grains due to the differing molar volumes of $CaCO_3$ and CaO. This results in an increasing diffusion resistance for CO_2, along with a reduction in porosity. Thus, diffusion through the product layer becomes the rate-limiting step.

In the software, the carbonation reaction is defined as a discrete particle reaction. A complete description of all the terms of the rate expression is reported in the Supplementary material.

A trial-and-error approach was used for tuning the kinetics according

Table 5
Literature reaction kinetics.

R1	$C(s) + H_2O \rightarrow CO + H_2$	$r_1 = \frac{k_{w1}[H_2O]}{1 + \left(k_{w1}/k_{w3}\right)[H_2O] + \left(k_{w2}/k_{w3}\right)[H_2]}$ $k_{w1} = 5342\ T\ exp\left(24500/T\right)$ $k_{w2} = 0.00785\ exp\left(6530/T\right)$ $k_{w3} = 1.64 \cdot 10^9\ exp\left(29200/T\right)$	[42,43]
R2	$C(s) + CO_2 \rightarrow 2CO$	$r_2 = \frac{k_{c1}[CO_2]}{1 + \left(k_{c1}/k_{c3}\right)[CO_2] + \left(k_{c2}/k_{c3}\right)[CO]}$ $k_{w1} = 1350\ exp\left(-22600/T\right)$ $k_{w2} = 0.0378\ exp\left(-10600/T\right)$ $k_{w3} = 8.83 \cdot 10^7\ exp\left(-27100/T\right)$	[43,44]
R3f	$CO + H_2O \rightarrow CO_2 + H_2$	$r_{3f} = 2.79\ exp\left(-1513/T\right)[CO][H_2O]$	[45]
R3r	$CO_2 + H_2 \rightarrow CO + H_2O$	$r_{3r} = 157.89\ exp\left(-910/T\right)[CO_2][H_2]$	[45]
R4	$CH_4 + H_2O \rightarrow CO + 3H_2$	$r_4 = 1.2863\ exp\left(-4350/T\right)[CH_4][H_2O]$	[45]
R5f	$0.5\ C(s) + H_2 \rightarrow 0.5CH_4$	$r_{5f} = 0.01368\ m_s T exp\left(-8078/T - 7.087\right)[H_2]$	[46]
R5r	$0.5CH_4 \rightarrow 0.5\ C(s) + H_2$	$r_{5r} = 0.151\ m_s T^{0.5} exp\left(-\frac{13578}{T} - 0.372\right)[CH_4]^{0.5}$	[46]
R6	$C_2H_4 + 2H_2O \rightarrow 2CO + 4H_2$	$r_6 = 0.12\ exp\left(-\frac{2058}{T}\right)[C_2H_4][H_2O]$	[47]
R7	$C_2H_6 + 2H_2O \rightarrow 2CO + 5H_2$	$r_7 = 0.12\ exp\left(-2058/T\right)[C_2H_6][H_2O]$	[47]
R8	$C_3H_8 + 3H_2O \rightarrow 3CO + 7H_2$	$r_8 = 0.12\ exp\left(-2058/T\right)[C_3H_8][H_2O]$	[47]
R9	$C_6H_6O + 5H_2O \rightarrow 6CO + 8H_2$	$r_9 = 8.25 \times 10^{11}\ exp\left(-24100/T\right)[C_6H_6O]$	[48]
R10	$C_7H_8 + 7H_2O \rightarrow 7CO + 11H_2$	$r_{10} = 51600\ exp\left(-10000/T\right)[C_7H_8]$	[48]
R11	$C_{10}H_8 + 10H_2O \rightarrow 10CO + 14H_2$	$r_{11} = 498.2\ exp\left(-5080/T\right)[C_{10}H_8]$	[48]
R12	$C_6H_6 + 6H_2O \rightarrow 6CO + 9H_2$	$r_{12} = \frac{k_{1_{C6H6}}[C_6H_6]}{1 + (k_{2_{C6H6}})[H_2] + (k_{3_{C6H6}})[H_2O]}$ $k_{1_{C6H6}} = 1.58 \cdot 10^{11}\ exp\left(-23700/T\right)$ $k_{2_{C6H6}} = 4.24 \cdot 10^{-7}\ exp\left(-12600/T\right)$ $k_{3_{C6H6}} = 6.99 \cdot 10^{-7}\ exp\left(-6520/T\right)$	[48]
R13	$C_6H_6 + H_2O \rightarrow 3C + 2CH_4 + CO$	$r_{13} = k_{4_{C6H6}}[C_6H_6][H_2O]^2$ $k_{4_{C6H6}} = 2 \cdot 10^{16}\ exp\left(-52923/T\right)$	[20]
R14	$CaO + CO_2 \rightarrow CaCO_3$	$r_{14} = \frac{N^0_{CaO}\sigma^0_{CaO}k_{CBN}(1 - X_{CaO})^{2/3}\left(C_{CO_2} - C_{CO_2,eq}\right)}{1 + \frac{N^0_{CaO}k_{CBN}}{2D_{pl}}\delta^0_{CaO}\sqrt[3]{1 - X_{CaO}}\left(1 - \sqrt[3]{\frac{1 - X_{CaO}}{1 - X_{CaO} + \varsigma \cdot X_{CaO}}}\right)}$	[49]

to the experimental results in BARRACUDA VR®. This method involves iteratively adjusting the activation energy parameters and comparing the predicted outcomes with experimental data to achieve the best fit.

2.4.3. 3D model of the lab-scale reactor

Fig. 3 shows the 3D model of the laboratory-scale reactor.

The main assumptions of the model are:

- Ash related reactions are neglected.
- Isothermal conditions: during the experimental tests a stable gasifier temperature was obtained by an electrical furnace.
- Aromatic compounds are grouped into the most abundant compounds: benzene, toluene and naphthalene.
- Reaction kinetics modified to reproduce the experimental test results, obtaining an engineering model for SEG.

Table 6 summarizes the simulation conditions.

A mesh size of 25,000 cells (corresponding to an average cell size of approximately 0.6 cm per side) was selected for the simulations to ensure accurate representation of the geometry while reducing the computational cost. A mesh sensitivity analysis was also performed, varying the cell size from 0.5 to 1.0 cm, to assess the impact of grid resolution on model predictions. The results of this analysis, reported in the Supplementary Materials, demonstrate that the mesh size does not significantly influence the simulation outcomes.

It is important to note that in the MP-PIC is crucial that each computational cell contains a statistically meaningful number of particles [50]. Therefore, cell sizes in the range of 0.5–1.0 cm, or even larger, are commonly adopted in CPFD simulations of fluidized bed gasifiers using Barracuda VR® [51–53].

Table 6
Operation condition set for simulation. The data referred to the test at steam to biomass ratio equal to 1 are reported in the brackets.

Reactor pressure (P)	1	bar
Reactor temperature (T)	670	°C
Steam to biomass ratio (S/B)	0.5 (1)	$wt_{fraction}$
Gas inlet temperature	550	°C
N_2 flux from the bottom	9.2 (3.2)	Nl/min
N_2 with feedstock injection	1.1	Nl/min
Olivine density	3300	kg/m^3
Dolomite density	2200	kg/m^3
Olivine Sauter mean diameter ($d_{3,2Olivine}$)	255e-6	m
Calcined dolomite Sauter mean diameter ($d_{3,2Calcined\ dolomite}$)	330e-6	m
Sand sphericity	0.73	–
Sand initial loading	≈3	kg
Close-pack volume fraction (ε)	0.6	–
Biomass feed rate	0.636	kg/h
Biomass density	700	kg/m^3
Biomass sphericity	1	–
Number of cells	Ranging between 7000 and 70,000	–
Maximum momentum redirection from collision	40 %	–
Normal-to-wall momentum retention	0.3	–
Tangent-to-wall momentum retention	0.995	–
Drag force	Wen-Yu & Ergun	–
Contact force model	Blended acceleration model	–
Turbulence model	(LES) Large eddy simulation	–

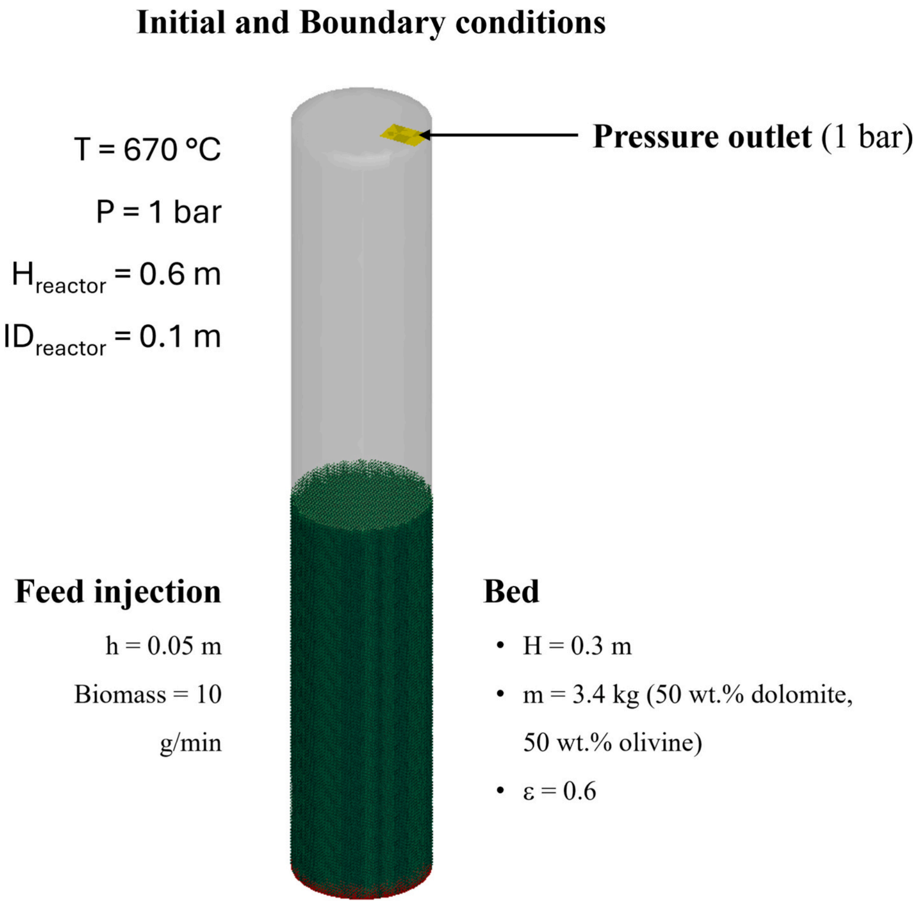

Fig. 3. Gasification reactor 3D model with initial and boundary conditions for simulation.

The mesh generated by the Barracuda VR® is a structured hexahedral mesh created through the Cartesian cut-cell method. Local mesh refinement near the walls is not feasible, and a uniform cell size must be employed throughout the domain. According to Zhang et al. [54], this constraint is not an issue in regions with high solids concentration, such as in a fluidized bed, where particles motion disrupts the development of a conventional fluid boundary layer. In these systems, the particle-laden boundary layer differs substantially from that in single-phase flows and is typically characterized by flow in the direction opposite to the bulk flow. As a result, when using the MP-PIC method, the near-wall region can be adequately described by focusing on the particle-phase behavior, with minimal concern for the gas flow. The high accuracy reported in previous MP-PIC simulations supports the validity of this assumption [55–59].

In addition, Barracuda VR® incorporates a sub-grid model to account for the modulation of turbulence induced by the presence of solid particles. This model significantly reduces the influence of turbulence as particle concentration increases, which is typical in dense-phase fluidized beds. Consequently, the turbulence structures observed in such flows differ markedly from those in single-phase LES, and mesh resolution requirements can be accordingly relaxed [60].

The near-wall resolution was evaluated by calculating the non-dimensional wall distance (y^+), confirming that an appropriate resolution is achieved (see Supplementary Materials). The results indicate that the turbulent region is confined to a relatively narrow central zone ($R <$ 20 mm), while approximately 84 % of the reactor volume lies in an area where the fluid flow appears nearly laminar. This observation could raise concerns about a possible underestimation of momentum and scalar transport phenomena. However, in dense gas–solid systems such as bubbling fluidized beds, flow dynamics and mixing are not governed solely by gas-phase turbulence. Particle motion driven by bubble formation and collapse, particle collisions, and wake entrainment contributes significantly to mixing and transport within the reactor [61]. The introduction of reactive particles (such as biomass particles which produces endogenous bubbles throughout devolatilization [62]) into the fluidized bed can substantially influence the overall flow dynamics, altering both gas and particle velocity fields as well as modifying the turbulence intensity within the system [63].

Moreover, the MP-PIC method has been proven capable of capturing key features of bubbling fluidization, including bubble-induced mixing and solid circulation patterns consistent with experimental data [64,65]. Additional studies have confirmed that bubble wakes, particle–particle collisions, and recirculation flows promote effective dispersion and enhance radial mixing, particularly in dense beds [66].This behavior is further illustrated by velocity fields of both gas and particle phases (see Supplementary Fig. S1), which reveal the presence of well-defined convective structures and recirculating flows throughout the bed, including in regions with low gas-phase turbulence intensity. These flow patterns contribute to sustained momentum and scalar transport, supporting the assumption of effective mixing even outside the core turbulent region.

To further confirm the reliability of the simulation results and ensure that they are not dominated by sub-grid modelling, the resolved fraction of turbulent kinetic energy (TKE) was calculated. This analysis also ensures that gas-phase reaction kinetics are not adversely affected by unresolved mixing phenomena. A representative domain slice with contours of the resolved TKE fraction is provided in the Supplementary Materials, showing that >80 % of the turbulence is indeed resolved across most of the reactor core.

A constant mass flow rate boundary condition was imposed, and the inlet velocity was calculated by distributing the measured flow uniformly over the inlet surface.

To evaluate the influence of modelling parameters on simulation results a sensitivity analysis was carried out varying the number of mesh cells, the turbulence model, and the Maximum momentum redirection from collision. The mesh resolution was altered by modifying the cell size within the range previously discussed, while different turbulence modelling approaches available in Barracuda VR® were tested to examine their influence under dense-phase flow conditions (LES, Algebraic and without turbulence model). Additionally, the Maximum momentum redirection from collision parameter was adjusted between 30 and 50 % to evaluate its role in particle dynamics and mixing behavior. The results of this sensitivity analysis are summarized in Table S1 (see Supplementary Materials) and confirm the robustness of the simulation outcomes.

3. Results and discussion

3.1. Devolatilization

Fig. 4 shows the devolatilization times as function of operating temperature, derived from batch tests.

A notable reduction in thermal degradation time by over 40 % is observed as the temperature increases from 600 to 850 °C. The observed trends in devolatilization times are consistent with previous studies [41], where an increase in temperature similarly led to a significant reduction in devolatilization times due to enhanced reaction kinetics.

The kinetic parameters were determined by fitting experimental devolatilization times using the Matlab DEV_Model, as developed in a previous study [28].

The mathematical model developed in Matlab employs the solution of the partial differential heat transfer equation in spherical coordinates to determine the temperature profile within a biomass heated in the fluidized bed, where both convective and radiative heat exchange occurs. The computed temperature profile over time is then used as the basis for determining the kinetic parameters featured in the equation. By imposing the constraint based on experimentally derived devolatilization times, the model identifies these parameters through an iterative process.

The resulting first-order expression fundamentally incorporates heat transfer phenomena, supporting their implementation within the simulation software. Since the software represents particles as material points, this expression allows for the consideration of thermal effects that would otherwise be neglected under isothermal conditions, where particles are assumed to have no volume.

Firstly, the activation energy and pre-exponential factor were calculated using MATLAB solve function. This function allows solving systems of symbolic equations and provides numerically accurate solutions. For each experimental devolatilization time measured at a given temperature, solve was used to compute the kinetic parameters E_i and A_i that satisfy the Arrhenius-type expression. The same value of E_i was obtained at each temperature, whereas temperature dependent values were observed for the pre-exponential factor A_i. According to the kinetic expression implemented in the Barracuda software, a power law correlation was applied to fit the calculated A_i values. The results of the fitting are presented in Fig. 5, showing a coefficient of determination of $R^2 =$

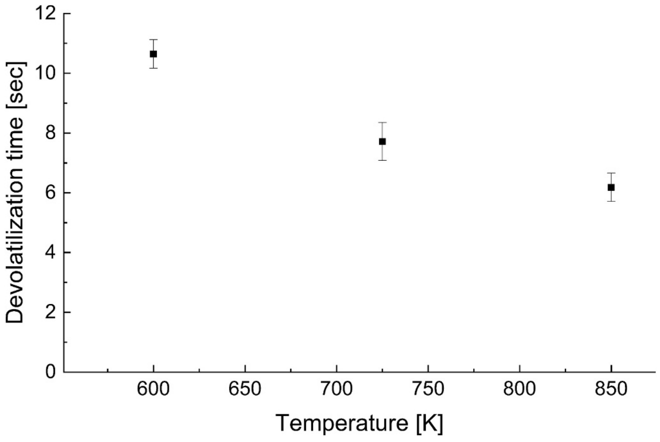

Fig. 4. Experimental devolatilization times.

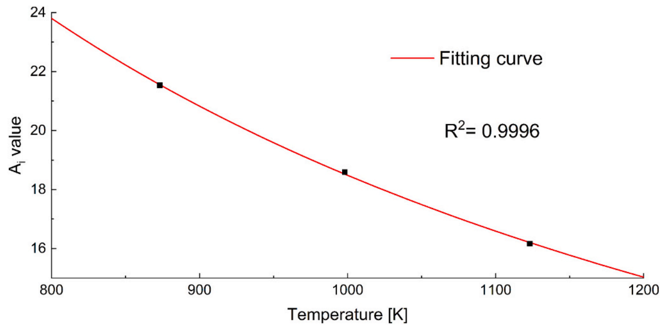

Fig. 5. Pre-exponential factor fitting curve.

0.9996.

The kinetic parameters obtained from the model are summarized in Table 7.

Fig. 6 shows the biomass conversion trend over time predicted by the model. The devolatilization times, calculated using kinetic parameters fitted to experimental data, are reported in the figure and compared with the experimental results. The relative differences remain below 2 %, confirming the accuracy of the model.

The distribution of the product released during the devolatilization step was determined through semi-continuous tests, as described in Section 2.2, which allowed the quantification of gas production, composition, tar content and residual char.

A summary of the results is reported in Table 8, while Fig. 7 shows the gas and aromatic compound compositions.

Analysis of the isopropanol samples highlights that toluene, naphthalene, phenol, and benzene are the main aromatic compounds produced. A detailed analysis of these products enables the calculation of the weight percentage distribution required for implementing devolatilization in CPFD software, as reported in Table 9.

3.2. Gasification

The gasifier reactor allows for the integration of a filter candle in the freeboard, enabling the use of a catalyst for in situ hot gas cleaning and conditioning [29]. However, in this study, the candle was left empty to focus on developing a model for sorption-enhanced gasification without catalytic improvement of the syngas. Nevertheless, the use of the filter candle prevents the elutriation of dolomite from the reactor [29], while also enhancing H_2-rich syngas production through CO_2 adsorption [67].

The gas composition trend during SEG, calcination and combustion phases of the tests is reported in Fig. 8, test #1 at S/B = 1 was chosen to be displayed (other results in Supplementary).

Two steam-to-biomass ratios were used for the tests in order to tune and validate the CPFD model. A summary of the experimental results is reported in Table 10.

By analyzing the results obtained in the two tests, significant differences emerge compared to those achievable in standard gasification (at 850 °C) and also based on the 'steam to biomass' (S/B) ratio, which influences both the gas yield and the chemical composition of the produced syngas, as shown in Fig. 9.

Table 7
Kinetic parameters for the devolatilization phase (see Eq. (4)).

Parameter	Value	Unit
B_i	45,701.06	–
C_i	−1.13	–
E_i	27,434.80	J/mol

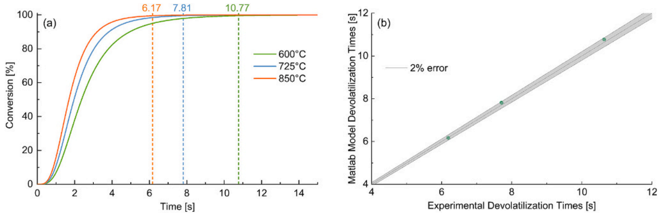

Fig. 6. Particle mass conversion trend over time predicted by the model, including the devolatilization times derived with the fitted kinetic parameters.

Table 8
Experimental results for the devolatilization phase.

Gas yield	0.45	Nl/g_{pellet}
Char	13.9	wt%
Tar	189.8	g/Nm^3_{gas}

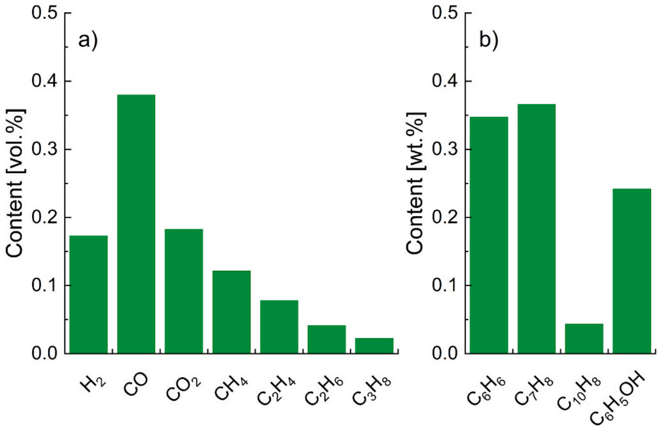

Fig. 7. Devolatilization products distribution: a) Gas composition (vol%); b) Aromatic compounds (wt%).

In Test #2, a water conversion of 40.8 % was observed, which is higher than the 29.5 % recorded in Test #1. However, despite the higher water conversion, Test #2 shows a lower gas yield of 0.76 Nm^3/kg of biomass than the higher yield of 0.80 Nm^3/kg in Test #1. This suggests that a higher S/B ratio favors biomass conversion, increasing the efficiency of the process [1]. This result is further supported by the char yield, which is 36 % in Test #1, lower than that in Test #2.

In both tests the char yield is significantly higher than what can be achieved in standard gasification, given the operating temperature. At elevated temperatures, the reaction becomes more favorable both thermodynamically and kinetically [68].

While the reduced char conversion efficiency may result in lower gas

Table 9
Percentage composition of devolatilization products.

Species	wt%
Volatiles	84.2
Char	13.9
Ash	2.0
H_2	0.8
CO	25.2
CO_2	19.0
CH_4	4.6
H_2O	29.8
C_2H_4	5.2
C_2H_6	3.0
C_3H_8	2.4
C_6H_6	3.5
C_7H_8	3.7
$C_{10}H_8$	0.4
C_6H_5OH	2.4

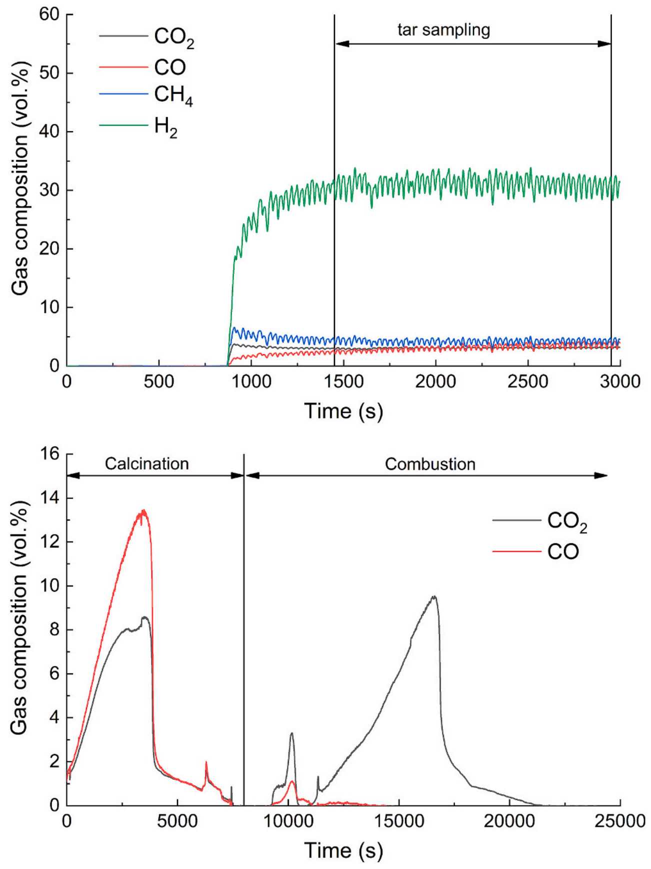

Fig. 8. Composition of the gas during the phases of Test #1.

Table 10
Experimental results for gasification phase.

	Test #1	Test #2
S/B	1.0	0.5
Gas yield (Nl/g_{pellet})	0.80	0.76
Char yield (wt%)	36.0 %	39.6 %
Tar (g/Nm^3_{gas})	11.6	9.5
Water conversion (wt%)	29.5 %	40.8 %

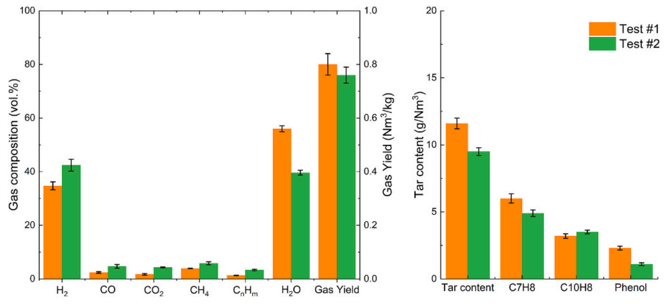

Fig. 9. Experimental results comparison in terms of gas and tar composition.

production (as it reflects less complete biomass conversion), it could also reduce the energy demand in a dual fluidized bed gasification process. In such a system, the residual char is transported to the combustion zone along with the bed material, where it is burned to calcine, the calcium carbonate formed during SEG and to heat the bed material, indirectly supplying the heat required for the gasification process.

Analyzing the syngas composition on a dry basis and without nitrogen, a notable difference is observed in hydrogen (H_2) production. In Test #1, the H_2 concentration reaches 78.8 %, significantly higher than the 70.2 % in Test #2. Thus, Test #1 demonstrates greater efficiency in H_2 production, likely due to enhanced reforming reactions of methane and light hydrocarbons [69].

At the same time, the CO_2 content in the produced gas decreases from 7.0 % in Test #2 to 3.8 % in Test #1. This reduction indicates effective CO_2 capture during the process, contributing to maximizing H_2 formation. Additionally, carbon monoxide (CO) content decreases in Test #1 (5.6 %) compared to 7.7 % in Test #2, suggesting that the different S/B ratio influences the water-gas shift reaction, promoting the CO conversion and H_2 production.

The concentrations of methane (CH_4) and light hydrocarbons (C_nH_m) also decrease in Test #1, with values of 8.9 % and 2.9 %, respectively, compared to the higher values in Test #2 (9.6 % CH_4 and 5.4 % C_nH_m). This suggests that a higher S/B ratio more strongly promotes the cracking and reforming reactions of hydrocarbons, leading to cleaner and more H_2-rich gas production.

An additional essential aspect is the tar content in the produced gases. One advantage of using sorbents such as dolomite is their catalytic effect on the thermal cracking reactions of heavy aromatic compounds. In Test #2, the tar content was 9.5 g/Nm^3, while in Test #1, it increased to 11.6 g/Nm^3. These values are similar to or lower than those typically obtained in standard gasification tests without the use of catalytic materials, confirming the effectiveness of dolomite in promoting tar cracking and conversion [69].

In summary, although Test #1 had a lower water conversion, it demonstrates better results in terms of gas production and syngas quality, with higher hydrogen production and reduced carbon-based compounds and solid residues. Test #2, while having lower tar content and higher water conversion, was less efficient in hydrogen production and resulted in a higher amount of char.

3.3. Model results and validation

Based on the results from the gasification tests, reaction kinetics were tuned accordingly. The kinetic parameters of the considered reactions were adjusted to develop a model capable of reproducing the behavior observed in Test #1, while the outcomes of Test #2 were used for validation purposes (Table 11).

As a result of the tuning process, the reaction kinetic parameters have been modified to better align model predictions with experimental results. Among these modifications, the kinetic of water-gas shift reaction was found to be increased by a factor of 10. This adjustment aligns with similar findings reported in previous studies, where pre-exponential factor of the WGS was adapted for sorption enhanced water gas shift simulation, leaving the activation energy unchanged [70,71].

The same procedure was also applied to the other compounds. In particular, for heavy hydrocarbons, the tuned values result within the range of variability reported in the literature, where various reaction pathways and kinetic expressions for tar cracking and reforming are described [72–75]. A simple kinetic model was chosen and the corresponding parameters were adjusted to reproduce the experimental results.

Figs. 10 and 11 compare the gas composition obtained in the two tests and their corresponding simulations in terms of gas yield, composition, and tar content. The analysis of the results indicates that the model can accurately predict biomass gasification behavior. The most significant discrepancies are found in the tar content, particularly in the concentrations of toluene and phenol, as shown in Fig. 9.

Fig. 10 shows the results obtained from CPFD simulations during the kinetics fitting phase, demonstrating good agreement with experimental data in terms of gas and tar prediction using both homogeneous and heterogeneous kinetics.

Moreover, the figure compares the simulations results obtained with the three mesh grids to assess their effect on the simulation. The results of sensitivity analysis.

Table 11
Reaction kinetics implemented in the simulation.

R1	$r_1 = \dfrac{k_{w1}[H_2O]}{1+\left(k_{w1}/k_{w3}\right)[H_2O]+\left(k_{w2}/k_{w3}\right)[H_2]}$
	$k_{w1} = 5342\,T\,exp\left(24500/T\right)$
	$k_{w2} = 0.00785\,exp\left(6530/T\right)$
	$k_{w3} = 1.64{\cdot}10^9\,exp\left(29200/T\right)$
R2	$r_2 = \dfrac{k_{c1}[CO_2]}{1+\left(k_{c1}/k_{c3}\right)[CO_2]+\left(k_{c2}/k_{c3}\right)[CO]}$
	$k_{w1} = 1350\,exp\left(-22600/T\right)$
	$k_{w2} = 0.0378\,exp\left(-10600/T\right)$
	$k_{w3} = 8.83{\cdot}10^7\,exp\left(-27100/T\right)$
R3f	$r_{3f} = 2.79\times 10\,exp\left(-1513/T\right)[CO][H_2O]$
R3r	$r_{3r} = 157.89\times 10\,exp\left(-910/T\right)[CO_2][H_2]$
R4	$r_4 = 1.2863\,exp\left(-4350/T\right)[CH_4][H_2O]$
R5f	$r_{5f} = 0.01368\,m_s Texp\left(-8078/T-7.087\right)[H_2]$
R5r	$r_{5r} = 0.151\,m_s T^{0.5} exp\left(-\dfrac{13578}{T}-0.372\right)[CH_4]^{0.5}$
R6	$r_6 = 0.24\,exp\left(-\dfrac{2058}{T}\right)[C_2H_4][H_2O]$
R7	$r_7 = 0.24\,exp\left(-2058/T\right)[C_2H_6][H_2O]$
R8	$r_8 = 0.24\,exp\left(-2058/T\right)[C_3H_8][H_2O]$
R9	$r_9 = 3.55\times 10^{12}\,exp\left(-24100/T\right)[C_6H_6O]$
R10	$r_{10} = 5.8\times 10^5\,exp\left(-10000/T\right)[C_7H_8]$
R11	$r_{11} = 274.2\,exp\left(-5080/T\right)[C_{10}H_8]$
R12	$r_{12} = \dfrac{k_{1_{C6H6}}[C_6H_6]}{1+\left(k_{2_{C6H6}}\right)[H_2]+\left(k_{3_{C6H6}}\right)[H_2O]}$
	$k_{1_{C6H6}} = 1.58{\cdot}10^{11}\,exp\left(-23700/T\right)$
	$k_{2_{C6H6}} = 4.24{\cdot}10^{-7}\,exp\left(-12600/T\right)$
	$k_{3_{C6H6}} = 6.99{\cdot}10^{-7}\,exp\left(-6520/T\right)$
R13	$r_{13} = k_{4_{C6H6}}[C_6H_6][H_2O]^2$
	$k_{4_{C6H6}} = 2{\cdot}10^{16}\,exp\left(-52923/T\right)$
R14	$r_{14} = \dfrac{N^0_{CaO}\sigma^0_{CaO}k_{CBN}(1-X_{CaO})^{2/3}\left(C_{CO_2}-C_{CO_2,eq}\right)}{1+\dfrac{N^0_{CaO}k_{CBN}}{2D_{pl}}\delta^0_{CaO}\sqrt[3]{1-X_{CaO}}\left(1-\sqrt[3]{\dfrac{1-X_{CaO}}{1-X_{CaO}+\varsigma{\cdot}X_{CaO}}}\right)}$

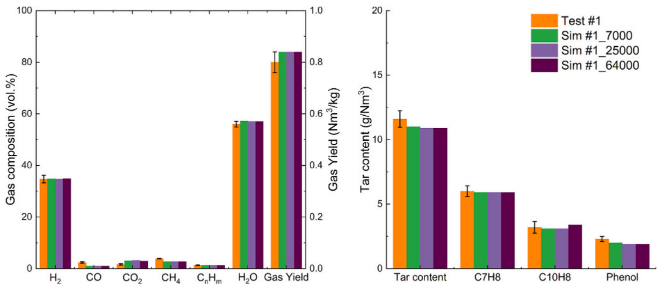

Fig. 10. Experimental data and simulation results (with 7000, 25000 and 64,000 cells mesh) comparison in terms of gas and tar composition after kinetic tuning.

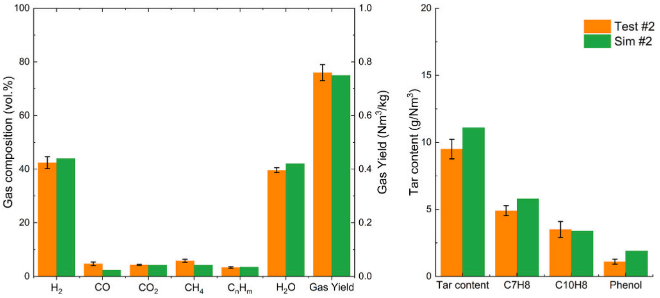

Fig. 11. CPFD model validation.

As highlighted by Fig. 10, the use of a higher resolution grid does not significantly affect the results, demonstrating its negligible impact. For this reason, the 25,000 cells mesh size was chosen to reduce the computational cost.

Fig. 11, meanwhile, presents a comparison, for verification purposes, between the previously calibrated kinetics of the CPFD model and the additional experimental results obtained at a different steam-to-carbon ratio.

During the verification phase, a discrepancy was observed primarily tar yield and composition prediction. This behavior is likely due to the selected kinetics for these compounds, whose formation and rearrangement processes are challenging to accurately model [76].

In the current CPFD modelling, only steam reforming kinetics were applied to heavy hydrocarbons, with thermal cracking considered for benzene only. Literature reports more complex models for tar, incorporating thermal cracking, steam reforming, and more intricate molecular recombination processes in parallel, which might help account for the observed differences [77].

Future simulations are planned to achieve this, implementing more advanced models involving heavy hydrocarbons reaction and rearrangement.

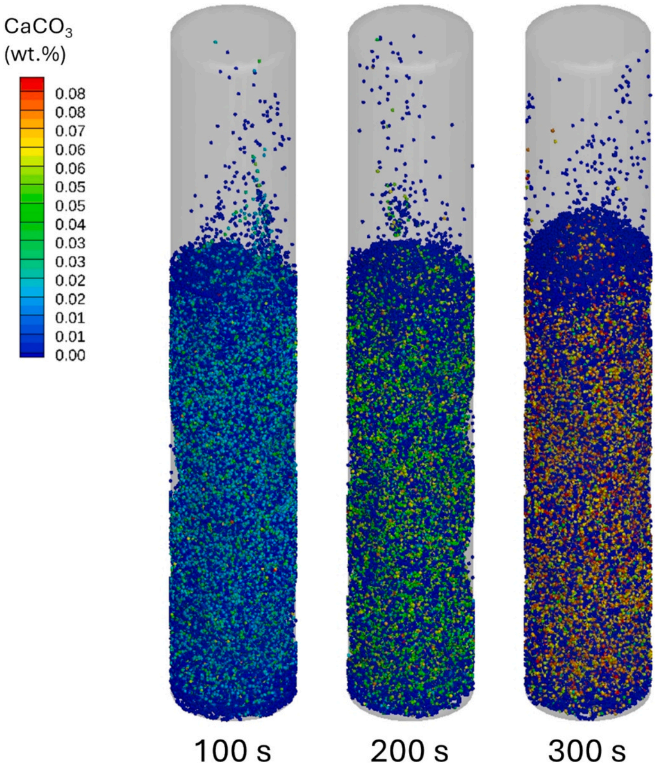

Fig. 12. Weight percentage of CaCO₃ in the bed at various simulation times from the CPFD simulation of Test #1.

Figs. 12–16 complete the results obtained from the model (Sim #1) by illustrating the behavior of the gases and solids inside the reactor as the simulation progresses (Figures related to Sim #2 are reported in Supplementary materials).

Fig. 12 shows the sorbent distribution within the bed and its mixing with the inert material, demonstrating the absence of segregation, which aligns with observation in the real case.

Fig. 15 presents the evolution of H_2, CO_2 and H_2O in the bed and freeboard of the reactor. The capture of CO_2 by the sorbent material shifts the water gas shift reaction equilibrium towards hydrogen production, followed by its partial regeneration in the freeboard region before leaving the reactor. These phenomena lead to cascading effects on H_2O and CO production and consumption.

Moreover, the model effectively predicts the $CaCO_3$ formation and thus the CO_2 captured during the SEG tests. In fact, under both conditions, the discrepancy between the CO_2 captured, calculated from the data in Fig. 8, and the value obtained from the simulation is <6 %.

These results demonstrate the model's effectiveness in accurately simulating the SEG process and its utility in reactor development by studying recirculation and calcination rate of $CaCO_3$ in a dual fluidized bed system.

4. Conclusions

The three-dimensional CPFD model developed in this study has proven to be a reliable tool for predicting the behavior of sorption-enhanced gasification (SEG), capturing key trends in hydrogen yield, gas composition, and calcium oxide carbonation. The gasification tests confirm the positive effect of CO_2 capture on syngas quality. During the gasification phase, CO_2 capture efficiency was demonstrated by a reduced syngas CO_2 content, contributing to an increased hydrogen production up to 79 vol%.

The model demonstrated its capacity to simulate key aspects of the SEG process, with only minor discrepancies in predicting tar formation.

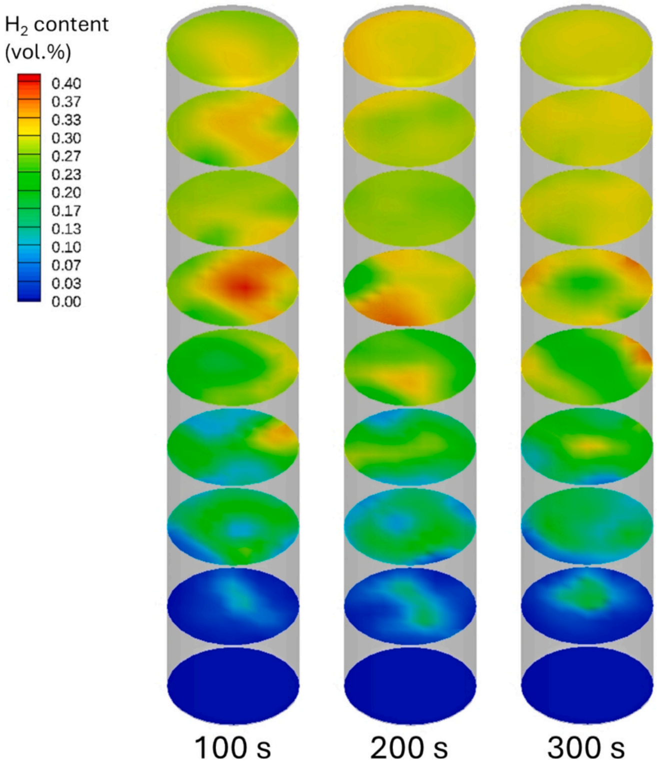

Fig. 13. Time and spatial evolution of H_2 during the CPFD simulation of Test#1.

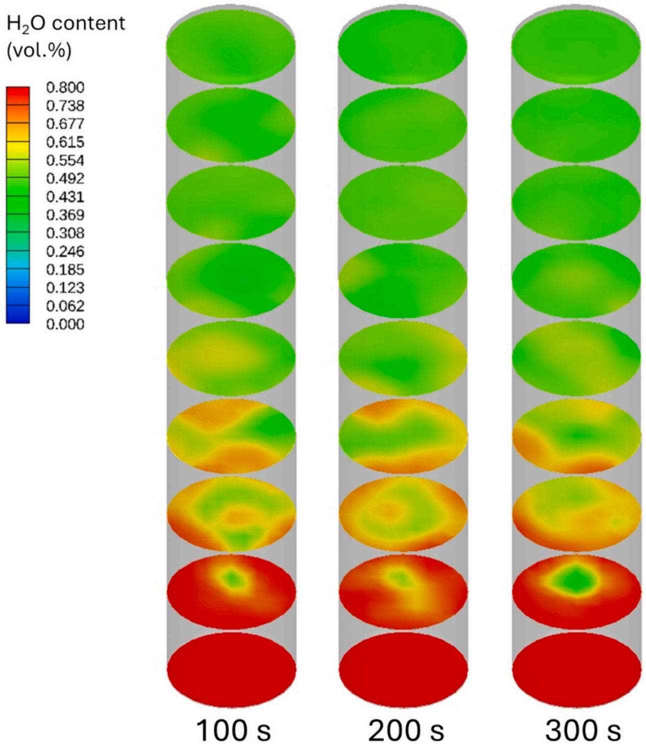

Fig. 14. Time and spatial evolution of H_2O during the CPFD simulation of Test#1.

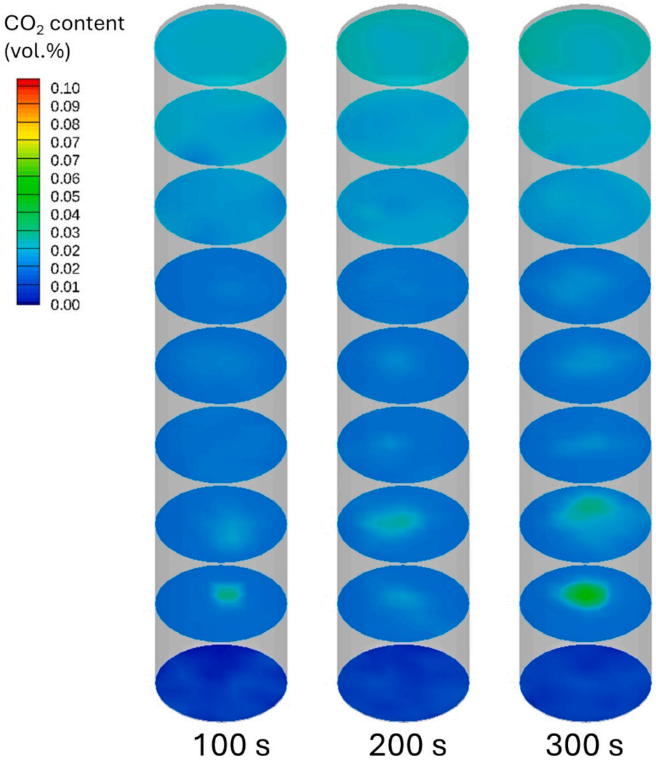

Fig. 15. Time and spatial evolution of CO_2 during the CPFD simulation of Test#1.

Overall, this study confirms that the CPFD model is a useful tool for supporting the development of fluidized bed reactor designs and optimizing operating conditions. Its capability to predict critical

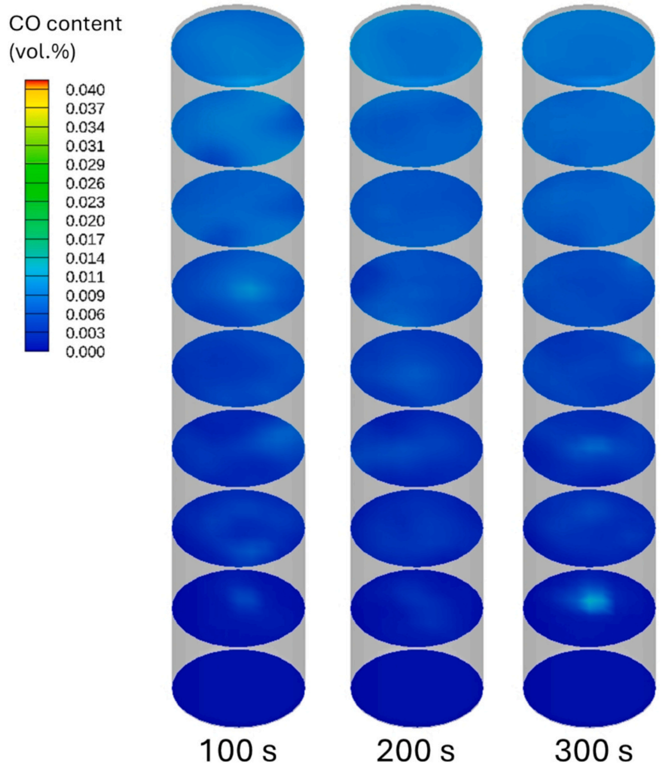

Fig. 16. Time and spatial evolution of CO during the CPFD simulation of Test#1.

performance metrics such as gas yield, CO_2 capture, and sorbent consumption establishes it as a valuable resource for scaling up SEG processes and enhancing the sustainability of hydrogen-rich syngas production. Future work will focus on refining the model, particularly regarding the kinetics of hydrocarbon reactions and tar formation, to further enhance its accuracy and practical applicability in reactor design and optimization.

CRediT authorship contribution statement

Alessandro Antonio Papa: Visualization, Validation, Supervision, Software, Methodology, Investigation, Formal analysis, Data curation, Conceptualization, Writing – review & editing, Writing – original draft. **Armando Vitale:** Visualization, Validation, Software, Methodology, Investigation, Data curation, Conceptualization, Writing – review & editing, Writing – original draft. **Umberto Pasqual Laverdura:** Resources, Project administration, Investigation, Writing – review & editing, Writing – original draft. **Antonio Di Nardo:** Visualization, Formal analysis, Writing – review & editing. **Giorgio Calchetti:** Visualization, Formal analysis, Writing – review & editing. **Andrea Di Carlo:** Supervision, Resources, Project administration, Methodology, Funding acquisition, Conceptualization, Writing – review & editing, Writing – original draft. **Sergio Rapagnà:** Supervision, Resources, Methodology, Investigation, Data curation, Writing – review & editing.

Declaration of competing interest

The authors declare that they have no known competing financial interests or personal relationships that could have appeared to influence the work reported in this paper.

Acknowledgments

The computing resources and the related technical support used for this work have been provided by CRESCO/ENEAGRID High Performance Computing infrastructure and its staff [52]. CRESCO/ENEAGRID High Performance Computing infrastructure is funded by ENEA, the Italian National Agency for New Technologies, Energy and Sustainable Economic Development and by Italian and European research programs, see http://www.cresco.enea.it/english for information. We also want to thank Eng. Federico Monterosso (OMIQ s.r.l.) for the technical support about Barracuda VR®. Electric System Research Programme, Project 1.6 “Energy Efficiency of Industrial Products and Processes”, WP 4 “Production of green H2 from biomass gasification using efficient CO2 capture, storage and reuse processes (PTR22-24)” and WP3 “Development of CCS for the efficiency of the HtA industry and the achievement of the Net-Zero objectives (PTR25-27)”, financed by the Ministry for the Environment and Energy Security.

Appendix A. Nomenclature

Symbol	Property	Unit
a_p	Particle acceleration	$m\ s^{-2}$
C_D	Drag coefficient	–
D_p	Inter-phase drag function	s^{-1}
F	Interphase momentum exchange rate	$kg\ m^{-2}\ s^{-2}$
f_d	Particle probability distribution function	–
m_p	Particle mass	kg
p	Pressure	Pa
P_s	Modelling constant in equation	Pa
r_p	Particle radius	m
t	Time	s^{-1}
T_p	Particle temperature	K
u_g	Gas velocity	m/s
u_p	Particle velocity	m/s
V_p	Volume of solid phase	m^3
α	Modelling constants	–
β	Modelling constant	–
ε_{cp}	Particle volume fraction at close-pack	–
ε_g	Gas volume fraction	–
ρ_g	Gas density	$kg\ m^{-3}$
ρ_p	Particle density	$kg\ m^{-3}$
τ	Inter-particle stress	Pa
τ_g	Fluid stress tensor	Pa

Appendix B. Supplementary data

Supplementary data to this article can be found online at https://doi.org/10.1016/j.cej.2025.165913.

Data availability

Data will be made available on request.

References

[1] L. Bartolucci, E. Bocci, S. Cordiner, E. De Maina, F. Lombardi, V. Marcantonio, P. Mele, V. Mulone, D. Sorino, Biomass polygeneration system for the thermal conversion of softwood waste into hydrogen and drop-in biofuels, Energies 16 (2023) 1286, https://doi.org/10.3390/EN16031286.

[2] A. Gallifuoco, A.A. Papa, A. Spera, L. Taglieri, A. Di Carlo, Dynamics of liquid-phase platform chemicals during the hydrothermal carbonization of lignocellulosic biomass, Bioresour. Technol. Rep. 19 (2022) 101177, https://doi.org/10.1016/J.BITEB.2022.101177.

[3] Net Zero by 2050 – Analysis - IEA, (n.d.). https://www.iea.org/reports/net-zero-by-2050 (accessed November 18, 2024).

[4] M. Binder, M. Kraussler, M. Kuba, M. Luisser, Hydrogen from biomass gasification. http://task33.ieabioenergy.com/content/Task%2033%20Projects, 2018. (Accessed 12 March 2023).

[5] A.A. Papa, A. Tacconi, E. Savuto, E. Ciro, A. Hatunoglu, P.U. Foscolo, L. Del Zotto, B. Aydin, E. Bocci, A. Di Carlo, Performance evaluation of an innovative 100 kWth dual bubbling fluidized bed gasifier through two years of experimental tests: results of the BLAZE project, Int. J. Hydrog. Energy 48 (2023) 27170–27181, https://doi.org/10.1016/J.IJHYDENE.2023.03.439.

[6] L. Marchetti, M. Guastaferro, F. Annunzi, L. Tognotti, C. Nicolella, M. Vaccari, Two-stage thermal pyrolysis of plastic solid waste: set-up and operative conditions investigation for gaseous fuel production, Waste Manag. 179 (2024) 77–86, https://doi.org/10.1016/J.WASMAN.2024.03.011.

[7] J. Fuchs, J.C. Schmid, S. Müller, H. Hofbauer, Dual fluidized bed gasification of biomass with selective carbon dioxide removal and limestone as bed material: a review, Renew. Sust. Energ. Rev. 107 (2019) 212–231, https://doi.org/10.1016/J.RSER.2019.03.013.

[8] O. Palone, A. Hoxha, G.G. Gagliardi, F. Di Gruttola, S. Stendardo, D. Borello, Synthesis of methanol from a chemical looping syngas for the decarbonization of the power sector, J. Eng. Gas Turbines Power 145 (2023), https://doi.org/10.1115/1.4055356/1145771.

[9] B. Vincenti, F. Gallucci, E. Paris, M. Carnevale, A. Palma, M. Salerno, C. Cava, O. Palone, G. Agati, M.V.M. Caputi, D. Borello, Syngas quality in fluidized bed gasification of biomass: comparison between olivine and K-feldspar as bed materials, Sustainability 15 (2023) 2600, https://doi.org/10.3390/SU15032600.

[10] A. Sebastiani, F. Parrillo, F. Ardolino, U. Arena, S. Iannello, M. Materazzi, Modelling of oxygen-steam gasification of waste feedstock in industrial fluidized bed reactors, Chem. Eng. J. 506 (2025) 159763, https://doi.org/10.1016/J.CEJ.2025.159763.

[11] B. Li, C. Fabrice Magoua Mbeugang, D. Liu, S. Zhang, S. Wang, Q. Wang, Z. Xu, X. Hu, Simulation of sorption enhanced staged gasification of biomass for hydrogen production in the presence of calcium oxide, Int. J. Hydrog. Energy 45 (2020) 26855–26864, https://doi.org/10.1016/J.IJHYDENE.2020.07.121.

[12] J. Fuchs, S. Müller, J.C. Schmid, H. Hofbauer, A kinetic model of carbonation and calcination of limestone for sorption enhanced reforming of biomass, Int. J. Greenh. Gas Control 90 (2019) 102787, https://doi.org/10.1016/J.IJGGC.2019.102787.

[13] L. Han, Q. Wang, Z. Luo, N. Rong, G. Deng, H2 rich gas production via pressurized fluidized bed gasification of sawdust with in situ CO2 capture, Appl. Energy 109 (2013) 36–43, https://doi.org/10.1016/J.APENERGY.2013.03.035.

[14] J. Fuchs, J.C. Schmid, S. Müller, H. Hofbauer, Dual fluidized bed gasification of biomass with selective carbon dioxide removal and limestone as bed material: a review, Renew. Sust. Energ. Rev. 107 (2019) 212–231, https://doi.org/10.1016/J.RSER.2019.03.013.

[15] N. Afandi, M. Satgunam, S. Mahalingam, A. Manap, F. Nagi, W. Liu, R. Bin Johan, A. Turan, A. Wei-Yee Tan, S. Yunus, Review on the modifications of natural and industrial waste CaO based sorbent of calcium looping with enhanced CO2 capture capacity, Heliyon 10 (2024) e27119, https://doi.org/10.1016/J.HELIYON.2024.E27119.

[16] J. Cai, F. Yan, M. Luo, S. Wang, Highly stable CO2 capture performance of binary doped carbide slag synthesized through liquid precipitation method, Fuel 280 (2020) 118575, https://doi.org/10.1016/J.FUEL.2020.118575.

[17] X. Liang, H. Chen, Utilization of biomass to promote calcium-based sorbents for CO2 capture, Greenh. Gases: Sci. Technol. 11 (2021) 837–855, https://doi.org/10.1002/GHG.2083.

[18] J. Fuchs, S. Müller, J.C. Schmid, H. Hofbauer, A kinetic model of carbonation and calcination of limestone for sorption enhanced reforming of biomass, Int. J. Greenh. Gas Control 90 (2019) 102787, https://doi.org/10.1016/J.IJGGC.2019.102787.

[19] S. Kraft, F. Kirnbauer, H. Hofbauer, CPFD simulations of an industrial-sized dual fluidized bed steam gasification system of biomass with 8 MW fuel input, Appl. Energy 190 (2017) 408–420, https://doi.org/10.1016/J.APENERGY.2016.12.113.

[20] D. Tokmurzin, J.Y. Nam, S.J. Park, S.J. Yoon, T.Y. Mun, S.M. Yoon, J.H. Moon, J.G. Lee, D.H. Lee, H.W. Ra, M.W. Seo, Three-dimensional CFD simulation of waste plastic (SRF) gasification in a bubbling fluidized bed with detailed kinetic chemical model, Energy Convers. Manag. 267 (2022) 115925, https://doi.org/10.1016/J.ENCONMAN.2022.115925.

[21] X. Zhu, Z. Wang, R. Ocone, H. Wang, MP-PIC simulation on CO2 gasification of biomass in a pilot plant circulating fluidized bed gasifier, Fuel 332 (2023) 125992, https://doi.org/10.1016/J.FUEL.2022.125992.

[22] A. Vitale, A.A. Papa, A. Di Carlo, S. Rapagnà, Three-dimensional computational fluid-dynamic simulation of polypropylene steam gasification, Int. J. Hydrog. Energy (2024), https://doi.org/10.1016/J.IJHYDENE.2024.09.101.

[23] A. Di Nardo, E. Savuto, G. Calchetti, S. Stendardo, Computational particle fluid dynamics 3D simulation of the sorption-enhanced steam methane reforming process in a dual fluidized bed of bifunctional sorbent-catalyst particles, Powder Technol. 424 (2023) 118568, https://doi.org/10.1016/J.POWTEC.2023.118568.

[24] D. Kong, S. Wang, K. Luo, C. Hu, D. Li, J. Fan, Three-dimensional simulation of biomass gasification in a full-loop pilot-scale dual fluidized bed with complex geometric structure, Renew. Energy 157 (2020) 466–481, https://doi.org/10.1016/j.renene.2020.04.130.

[25] M. Guo, J. Yu, S. Wang, K. Luo, J. Fan, Study of biomass gasification combined with CO2 absorption in a dual fluidized bed (DFB) using the Eulerian-Lagrangian method, Chem. Eng. J. 483 (2024) 148723, https://doi.org/10.1016/J.CEJ.2024.148723.

[26] H. Liu, R.J. Cattolica, R. Seiser, C. hsien Liao, Three-dimensional full-loop simulation of a dual fluidized-bed biomass gasifier, Appl. Energy 160 (2015) 489–501, https://doi.org/10.1016/j.apenergy.2015.09.065.

[27] A. Vitale, A.A. Papa, S. Iannello, E. Ciro, A. Hatunoglu, V. Corradetti, N. Rovelli, P.U. Foscolo, A. Di Carlo, Devolatilization of polypropylene particles in fluidized bed, Energies 16 (2023) 6324, https://doi.org/10.3390/EN16176324.

[28] A. Vitale, A. Di Carlo, P.U. Foscolo, A.A. Papa, Kinetic model implementation of fluidized bed devolatilization, Energies 17 (2024) 3154, https://doi.org/10.3390/en17133154.

[29] A.A. Papa, E. Savuto, A. Di Carlo, A. Tacconi, S. Rapagnà, Synergic effects of bed materials and catalytic filter candle for the conversion of tar during biomass steam gasification, Energies 16 (2023) 595, https://doi.org/10.3390/EN16020595.

[30] M.J. Andrews, P.J. O'Rourke, The multiphase particle-in-cell (MP-PIC) method for dense particulate flows, Int. J. Multiphase Flow 22 (1996) 379–402, https://doi.org/10.1016/0301-9322(95)00072-0.

[31] D.M. Snider, An incompressible three-dimensional multiphase particle-in-cell model for dense particle flows, J. Comput. Phys. 170 (2001) 523–549, https://doi.org/10.1006/JCPH.2001.6747.

[32] A.A. Amsden, P.J. O'Rourke, T.D. Butler, KIVA-II: A Computer Program for Chemically Reactive Flows With Sprays, 1989, https://doi.org/10.2172/6228444.

[33] U. Piomelli, Large-eddy simulation: achievements and challenges, Prog. Aerosp. Sci. 35 (1999) 335–362, https://doi.org/10.1016/S0376-0421(98)00014-1.

[34] J. Smagorinsky, General circulation experiments with the primitive equations, Mon. Weather Rev. 91 (1963) 99, https://doi.org/10.1175/1520-0493(1963)091.

[35] C.W.-F.P. Technology, Chem.Eng. Progress, undefined 1966, Mechanics of fluidization, Cir.Nii.Ac.Jp (n.d.).

[36] Fluidization Engineering - D. Kunii, Octave Levenspiel - Google Libri, (n.d.). https://books.google.it/books?hl=it&lr=&id=ZVnb17qRz8QC&oi=fnd&pg=PR17&ots=xCgYRC-cGI&sig=-zwoGhxcqndwcwxO-HGclFIw4E8&redir_esc=y#v=onepage&q&f=false (accessed May 16, 2024).

[37] S.E. Harris, D.G. Crighton, Solitons, solitary waves, and voidage disturbances in gas-fluidized beds, J. Fluid Mech. 266 (1994) 243–276, https://doi.org/10.1017/S0022112094000996.

[38] P.J. O'Rourke, D.M. Snider, A new blended acceleration model for the particle contact forces induced by an interstitial fluid in dense particle/fluid flows, Powder Technol. 256 (2014) 39–51, https://doi.org/10.1016/J.POWTEC.2014.01.084.

[39] D. Tokmurzin, J.Y. Nam, S.J. Park, S.J. Yoon, T.Y. Mun, S.M. Yoon, J.H. Moon, J.G. Lee, D.H. Lee, H.W. Ra, M.W. Seo, Three-dimensional CFD simulation of waste plastic (SRF) gasification in a bubbling fluidized bed with detailed kinetic chemical model, Energy Convers. Manag. 267 (2022) 115925, https://doi.org/10.1016/j.enconman.2022.115925.

[40] T. Dymala, S. Wang, K. Jarolin, T. Song, L. Shen, M. Dosta, S. Heinrich, MP-PIC simulation of biomass steam gasification using ilmenite as an oxygen carrier, Atmosphere 13 (2022) 1009, https://doi.org/10.3390/ATMOS13071009.

[41] D. Neves, H. Thunman, A. Matos, L. Tarelho, A. Gómez-Barea, Characterization and prediction of biomass pyrolysis products, Prog. Energy Combust. Sci. 37 (2011) 611–630, https://doi.org/10.1016/J.PECS.2011.01.001.

[42] M. Barrio, B. Gøbel, H. Rimes, U. Henriksen, J.E. Hustad, L.H. Sørensen, Steam gasification of wood char and the effect of hydrogen inhibition on the chemical kinetics, in: Progress in Thermochemical Biomass Conversion, 2008, pp. 32–46, https://doi.org/10.1002/9780470694954.CH2.

[43] J. Konttinen, A. Moilanen, J. Vepsäläinen, S. Kallio, M. Hupa, E. Kurkela, Modelling and Experimental Testing of Gasification of Biomass Char Particles. http://www.abo.fi/fak/ktf/cmc/, 2003. (Accessed 21 October 2024).

[44] M. Barrio, J. Hustad, CO2 gasification of birch char and the effect of CO inhibition on the calculation of chemical kinetics, in: Progress in Thermochemical Biomass Conversion, 2008, pp. 47–60, https://doi.org/10.1002/9780470694954.CH3.

[45] Y. Wang, C.M. Kinoshita, Kinetic model of biomass gasification, Sol. Energy 51 (1993) 19–25, https://doi.org/10.1016/0038-092X(93)90037-O.

[46] M. Syamlal, L.A. Bissett, METC Gasifier Advanced Simulation (MGAS) Model, Other Information: PBD: Jan 1992, 1992, https://doi.org/10.2172/10127635.

[47] I. Barbarias, G. Lopez, M. Artetxe, A. Arregi, J. Bilbao, M. Olazar, Kinetic modeling of the catalytic steam reforming of high-density polyethylene pyrolysis volatiles, Energy Fuel 31 (2017) 12645–12653, https://doi.org/10.1021/ACS.ENERGYFUELS.7B01909.

[48] A. Di Carlo, D. Borello, E. Bocci, Process simulation of a hybrid SOFC/mGT and enriched air/steam fluidized bed gasifier power plant, Int. J. Hydrog. Energy 38 (2013) 5857–5874.

[49] S. Stendardo, P.U. Foscolo, Carbon dioxide capture with dolomite: a model for gas–solid reaction within the grains of a particulate sorbent, Chem. Eng. Sci. 64 (2009) 2343–2352, https://doi.org/10.1016/J.CES.2009.02.009.

[50] C.B. Solnordal, V. Kenche, T.D. Hadley, Y. Feng, P.J. Witt, K.S. Lim, Simulation of an internally circulating fluidized bed using a multiphase particle-in-cell method, Powder Technol. 274 (2015) 123–134, https://doi.org/10.1016/J.POWTEC.2014.12.045.

[51] B. Amblard, R. Singh, E. Gbordzoe, L. Raynal, CFD modeling of the coke combustion in an industrial FCC regenerator, Chem. Eng. Sci. 170 (2017) 731–742, https://doi.org/10.1016/J.CES.2016.12.055.

[52] S. Bai, X. Wang, H. Pan, R. Gou, Y. Yang, Y. Zhang, S. Li, Application of CPFD method in simulation of an industrial MTO regenerator, Chem. Eng. J. 505 (2025) 159348, https://doi.org/10.1016/J.CEJ.2025.159348.

[53] Y. Liang, Y. Zhang, T. Li, C. Lu, A critical validation study on CPFD model in simulating gas–solid bubbling fluidized beds, Powder Technol. 263 (2014) 121–134, https://doi.org/10.1016/J.POWTEC.2014.05.003.

[54] W. Zhang, F. Johnsson, B. Leckner, Fluid-dynamic boundary layers in CFB boilers, Chem. Eng. Sci. 50 (1995) 201–210, https://doi.org/10.1016/0009-2509(94)00222-D.

[55] Z. Bai, W. Hu, X. Zhu, S. Wang, Y. Gu, Solar-driven biomass steam gasification by new concept of solar particles heat carrier with CPFD simulation, Energy Convers. Manag. 293 (2023) 117500, https://doi.org/10.1016/J.ENCONMAN.2023.117500.

[56] S. Kraft, F. Kirnbauer, H. Hofbauer, CPFD simulations of an industrial-sized dual fluidized bed steam gasification system of biomass with 8 MW fuel input, Appl. Energy 190 (2017) 408–420, https://doi.org/10.1016/J.APENERGY.2016.12.113.

[57] Y. Jiang, G. Qiu, H. Wang, Modelling and experimental investigation of the full-loop gas-solid flow in a circulating fluidized bed with six cyclone separators, Chem. Eng. Sci. 109 (2014) 85–97, https://doi.org/10.1016/J.CES.2014.01.029.

[58] J. Parker, K. Lamarche, W. Chen, K. Williams, H. Stamato, S. Thibault, CFD Simulations for Prediction of Scaling Effects in Pharmaceutical Uidized Bed Processors at Three Scales, 2012, https://doi.org/10.1016/j.powtec.2012.09.021.

[59] J. Bigda, CPFD numerical study of impact dryer performance, Dry. Technol. 32 (2014) 1277–1288, https://doi.org/10.1080/07373937.2014.929586.

[60] V.R. Barracuda, Barracuda Virtual Reactor User Manual 2016, CPFD Software, LLC, Albuquerque, 2016.

[61] S. Wang, Y. Shen, CFD-DEM modelling of dense gas-solid reacting flow: recent advances and challenges, Prog. Energy Combust. Sci. 109 (2025) 101221, https://doi.org/10.1016/J.PECS.2025.101221.

[62] S. Iannello, D. Macrì, M. Materazzi, A comprehensive assessment of endogenous bubbles properties in fluidized bed reactors via X-ray imaging, Powder Technol. 413 (2023) 118013, https://doi.org/10.1016/J.POWTEC.2022.118013.

[63] H. Zhou, G. Flamant, D. Gauthier, DEM-LES of coal combustion in a bubbling fluidized bed. Part I: gas-particle turbulent flow structure, Chem. Eng. Sci. 59 (2004) 4193–4203, https://doi.org/10.1016/J.CES.2004.01.069.

[64] P.J. O'Rourke, D.M. Snider, Inclusion of collisional return-to-isotropy in the MP-PIC method, Chem. Eng. Sci. 80 (2012) 39–54, https://doi.org/10.1016/J.CES.2012.05.047.

[65] Z. Wan, S. Yang, H. Wang, MP-PIC investigation of the multi-scale gas-solid flow in the bubbling fluidized bed, Exp. Comput. Multiph. Flow 3 (2021) 289–302, https://doi.org/10.1007/S42757-020-0067-1. /METRICS.

[66] D. Kunii, O. Levenspiel, Fluidization Engineering, 2nd edition, 2013.

[67] A.M. Parvez, S. Hafner, M. Hornberger, M. Schmid, G. Scheffknecht, Sorption enhanced gasification (SEG) of biomass for tailored syngas production with in-situ CO2 capture: current status, process scale-up experiences and outlook, Renew. Sust. Energ. Rev. 141 (2021) 110756, https://doi.org/10.1016/J.RSER.2021.110756.

[68] M. Morin, S. Pécate, M. Hémati, Experimental study and modelling of the kinetic of biomass char gasification in a fluidized bed reactor, Chem. Eng. Res. Des. 131 (2018) 488–505, https://doi.org/10.1016/J.CHERD.2017.09.030.

[69] G. Soukup, C. Pfeifer, A. Kreuzeder, H. Hofbauer, In situ CO2 capture in a dual fluidized bed biomass steam gasifier – bed material and fuel variation, Chem. Eng. Technol. 32 (2009) 348–354, https://doi.org/10.1002/CEAT.200800559.

[70] J. Castro, J. Leaver, S. Pang, Kinetic modeling of the CaO-based sorption-enhanced water gas shift processing of biomass gasification producer gas, Biomass Convers. Biorefin. (2025) 1–14, https://doi.org/10.1007/S13399-025-06597-3/FIGURES/8.

[71] H. Rashidi, A. Duffy, W. Doherty, A detailed general model of the gasification zone of a dual fluidised bed gasifier, Biomass Convers. Biorefin. 1 (2022) 1–16, https://doi.org/10.1007/S13399-022-02529-7/FIGURES/18.

[72] M. Puig-Gamero, D.T. Pio, L.A.C. Tarelho, P. Sánchez, L. Sanchez-Silva, Simulation of biomass gasification in bubbling fluidized bed reactor using aspen plus®, Energy Convers. Manag. 235 (2021) 113981 https://doi.org/10.1016/J.ENCONMAN.2021.113981.

[73] A. Gómez-Barea, B. Leckner, Modeling of biomass gasification in fluidized bed, Prog. Energy Combust. Sci. 36 (2010) 444–509, https://doi.org/10.1016/J.PECS.2009.12.002.

[74] E. Savuto, A. Di Carlo, K. Gallucci, S. Stendardo, S. Rapagnà, 3D-CFD simulation of catalytic filter candles for particulate abatement and tar and methane steam reforming inside the freeboard of a gasifier, Chem. Eng. J. 377 (2019) 120290, https://doi.org/10.1016/J.CEJ.2018.10.227.

[75] H. Rashidi, A. Duffy, W. Doherty, A detailed general model of the gasification zone of a dual fluidised bed gasifier, Biomass Convers. Biorefin. 1 (2022) 1–16, https://doi.org/10.1007/S13399-022-02529-7/FIGURES/18.

[76] T.A. Milne, R.J. Evans, N. Abatzaglou, Biomass Gasifier "Tars": Their Nature, Formation, and Conversion, 1998, https://doi.org/10.2172/3726.

[77] Q. Li, Q. Wang, Y. Tsuboi, J. Zhang, J. Liu, Steam reforming of tar studied in bench-scale experiments and pilot-scale tests with simulations, Fuel 290 (2021) 120028, https://doi.org/10.1016/J.FUEL.2020.120028.